Ultrasmall Iron Oxide Nanoparticles for Biomedical Applications: Improving the Colloidal and Magnetic Properties

7 AUTHORS, INCLUDING:

Valentina Bello
University of Padova
63 PUBLICATIONS **703** CITATIONS

SEE PROFILE

Caroline Robic
Guerbet Group
43 PUBLICATIONS **3,460** CITATIONS

SEE PROFILE

Marc Port
109 PUBLICATIONS **5,902** CITATIONS

SEE PROFILE

Maria del Puerto Morales
Instituto de Ciencia de Materiales de Madrid
254 PUBLICATIONS **7,991** CITATIONS

SEE PROFILE

Ultrasmall Iron Oxide Nanoparticles for Biomedical Applications: Improving the Colloidal and Magnetic Properties

Rocio Costo,[†] Valentina Bello,[‡] Caroline Robic,[§] Marc Port,[§] Jose F. Marco,[∥] M. Puerto Morales,[†] and Sabino Veintemillas-Verdaguer*,[†]

[†]Instituto de Ciencia de Materiales de Madrid (CSIC), Sor Juana Inés de la Cruz 3, 28049 Madrid, Spain

[‡]Dipartimento di Fisica, Università di Padova, Via Marzolo 8, 35131 Padova, Italy

[§]Guerbet Research, BP 57400, 95943 Roissy CDG, France

[∥]Instituto de Química-Física Rocasolano (CSIC), Serrano 119, 28006 Madrid, Spain

ⓢ Supporting Information

ABSTRACT: A considerable increase in the saturation magnetization, M_s (40%), and initial susceptibility of ultrasmall (<5 nm) iron oxide nanoparticles prepared by laser pyrolysis was obtained through an optimized acid treatment. Moreover, a significant enhancement in the colloidal properties, such as smaller aggregate sizes in aqueous media and increased surface charge densities, was found after this chemical protocol. The results are consistent with a reduction in nanoparticle surface disorder induced by a dissolution—recrystallization mechanism.
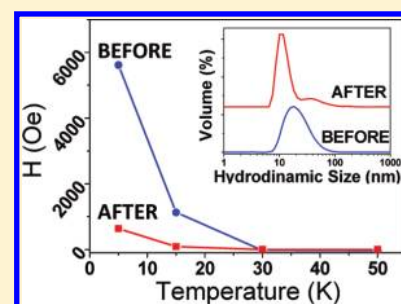
1. INTRODUCTION

During the last few decades, much has been written about the use of magnetic iron oxide nanoparticles for applications in magnetic storage, energy storage devices, biomedicine, and catalysis.[1−12] This increasing need for magnetic nanoparticles could be solved through high-performance techniques, such as synthesis methods based on condensation from the gas phase or the precipitation of salts in an aqueous medium. These synthesis pathways might produce large quantities of ultrasmall nanoparticles. However, for real industrial applicability, especially in the case of biomedical applications, it is necessary to overcome a series of difficulties such as the high tendency to aggregate or the poor magnetization of the smallest nanoparticles.

One of the main problems with ultrasmall iron oxide nanoparticles is surface disorder.[13−17] Atoms at the surface have fewer neighbors than atoms in the bulk.[18] Because of this lower coordination and unsatisfied bonds, atoms at the surface are less ordered than bulk atoms, which has a direct impact on the particle's properties (i.e., the magnetic properties). It is possible to use several approaches to overcome this problem, for instance, the use of a surfactant that is linked to the particle surface. In this case, it is possible to take advantage of the interplay of the surface cations on the particles and the ligand of the surfactant, leading to saturation magnetization close to that in the bulk.[19] However, this strategy is useless when direct biomedical applications are pursued. In this case, water-stable surfactant-free nanoparticles are preferred. Thus, new approaches to reduce the disorder at the ultrasmall iron oxide nanoparticle surface in an aqueous medium

are needed. Moreover, in biology, excess Fe(II) is believed to generate oxidative stress, which is understood as an increase in the steady-state concentration of oxygen radical intermediates. This stress is harmful for cells and is involved in many diseases.[20,21] Thus, a protocol to oxidize the likely Fe(II) present in iron oxide nanoparticles is required to obtain safer and more stable particles for biomedical applications.

In this work, we used a gas-phase synthesis method—laser pyrolysis—that produces very high quality, ultrasmall nanoscale particles (<5 nm) with rather spheroid morphology and exceptionally narrow particle size distributions. Furthermore, laser pyrolysis is one of the most convenient synthesis processes because it enables the production of nanoparticles in a continuous way with low cost and with no use of surfactants or hazardous additives.[22] However, as with most of the gas-phase routes, nucleation is very fast and particles have no time to grow or properly crystallize. As a result, particles prepared by laser pyrolysis are usually smaller and less crystalline than those prepared by other synthesis routes.

Here, we report an optimized oxidizing protocol to improve the magnetic properties and colloidal stability of ultrasmall iron oxide magnetic nanoparticles through the reduction of particle surface disorder. This procedure, referred to as acid treatment, is based on an oxidation—dispersion protocol previously reported

by several authors.[23−26] Although the initial treatment was expected to be superfluous for the smallest particles,[24] we have optimized the procedure to make it exceptionally efficient and have studied this treatment in detail. Through a series of partial dissolution−recrystallization steps, we enhanced both the colloidal and magnetic properties. A complete structural, colloidal, and magnetic characterization of the samples before and after acid treatment was carried out to verify the success of the procedure, and the results were compared with those for acid-treated particles prepared by coprecipitation. We related the observed enhancement in magnetic and colloidal properties to the reduction in particle surface disorder.

2. EXPERIMENTAL SECTION

2.1. Materials. Iron oxide magnetic nanoparticles were synthesized by laser pyrolysis (sample L) and the coprecipitation of salts in an aqueous medium (sample C) following previously described procedures.[27−29] Coprecipitated particles were prepared for comparison purposes because they have been widely studied in the past and there are many references to these particles in the literature.[17,28]

Sample L was synthesized using the laser-induced pyrolysis of iron pentacarbonyl $Fe(CO)_5$ vapors, following methods described in the literature.[29−31] The experimental synthesis conditions were the following: 10 °C precursor temperature, 60 W continuous wave (CW) CO_2 laser power, 3.5 mm laser spot diameter, 400 mbar pressure, 1726 sccm ($cm^3 min^{-1}$ at 0 °C 1.01 bar absolute) Ar window flux, 105 sccm Ar axial flux, and a carrier gas flux formed by a mixture of 12 sccm C_2H_4 and 75 sccm air (hard oxidation).

Sample C corresponds to iron oxide nanoparticles synthesized in an aqueous medium. For this purpose, 75 mL of an aqueous NH_3 solution (25%) was rapidly added to a solution of $FeCl_2$ (0.175 M) and $FeCl_3$ (0.334 M). The addition was carried out at room temperature under vigorous stirring. After 5 min, the sample was washed three times with distilled water by magnetic decantation.

Both samples were treated following an optimized acid treatment. Briefly, 350 mg of a dried sample was treated with 2 mL of HNO_3 (5 M) under sonication for 15 min. Then, 2 mL of $Fe(NO_3)_3$ (0.5 M) and 6 mL of water were added, and the mixture was boiled under reflux for 30 min. When the sample was cool, an additional 2 mL of HNO_3 (2 M) was added and the sample was treated under sonication for another 15 min. The last step consisted of washing the sample to remove excess acid either by centrifugation in the case of the largest samples (particles >5 nm) or by dialysis in the case of the smallest samples. The resulting laser and coprecipitation particles after treatment are referred to as L-AT and C-AT, respectively.

2.2. Characterization Techniques. The crystal structure of the samples was identified by X-ray powder diffraction performed in a Bruker D8 Advance powder diffractometer using Cu Kα radiation with an energy-discriminator (Sol-X) detector. The patterns were collected within 5 and 90° in 2θ. The XRD spectra were indexed to an inverse spinel structure. The average crystallite size was calculated by Scherrer's formula using the half width of the (311) X-ray diffraction peak using the utilities of the automatic powder diffraction computer program (APD) from Phillips for the separation of (311) and (400) peaks. The error in the crystallite sizes obtained by use of the Scherrer's formula is ±0.1 nm and is related to the instrumental line width of the diffractometer ($\Delta 2\theta = 0.11°$).

The particle size was determined from TEM micrographs using a 200 keV JEOL-2000 FXII microscope. For the observation of the sample in the microscope, the particles were dispersed in isopropanol and a drop of the suspension was placed onto a copper grid covered with a perforated carbon film. The mean particle size and distribution were evaluated by

measuring the largest internal dimension of at least 100 particles. Afterward, data were fitted to a log normal or Gaussian distribution by obtaining the mean size and standard deviation (σ) that were considered to be representative of the absolute error of the measurement. For some samples, the exposure of the region of interest to the electron beam was minimized by obtaining the best focus, astigmatism, and brightness on an adjacent region. Phase changes and sample damage can be induced by exposure to the microscope's electron beam.

High-resolution electron microscopy (HREM) observations were carried out in an FEI-Tecnai field-emission gun (FEG) TEM F-20 Super Twin operating at 200 keV and equipped with an EDAX energy-dispersive X-ray spectrometer (EDS). The images were Fourier filtered in order to minimize the contrast from the amorphous carbon support.

Infrared spectra of the samples diluted in 2% KBr were recorded between 4500 and 250 cm^{-1} in a Bruker IFS 66 V-S.

The magnetic properties of the samples were recorded in a vibrating sample magnetometer (MagLabVSM, Oxford Instrument). For the measurement of powders, the samples were dried in an inox-coated oven at 50 °C for 24 h. Afterward, the samples were accurately weighed and fitted into the sample holder. To minimize interactions in the liquid samples, the dispersions were prepared at low concentrations (0.25 wt %). To avoid nanoparticle aggregation due to the VSM magnetic field, liquid samples were always measured in the frozen state. One hundred microliters of the sample was placed in the sample holder and immersed in liquid nitrogen before being placed in the VSM. The temperature was always kept under 250 K. Temperature-dependent zero field cooling (ZFC) and field cooling (FC) magnetization measurements were taken by initially cooling the samples to 5 K in the zero and 200 Oe fields, respectively. Then, magnetization was measured during the heating cycle (3 K·min^{-1}) from 5 to 250 K under a 200 Oe field. Hysteresis loops of the powder samples were measured at RT and at 5 K at a rate of 5 kOe·min^{-1}. The saturation magnetization was evaluated by extrapolating the experimental data obtained in the high-field range to an infinite field; in the high-field range, the magnetization increases linearly with H, which can be approximated to a $1/H$ law. Exchange anisotropy studies were undertaken by holding the sample at 5 K in a 50 kOe field. Afterward, hysteresis loops were carried out at 5 kOe·min^{-1}.

Simultaneous thermogravimetric (TG) analysis and differential thermal analysis (DTA) were performed on a Seiko TG/DTA 320U thermobalance. Samples were heated from room temperature to 900 °C at 10 °C/min under an air flow of 100 mL/min.

Iron determination was carried out in an inductively coupled plasma-optical emission spectrometry (ICP-OES) apparatus from Perkin-Elmer (model OPTIME 2100DV). The determination of the carbon content was carried out in a Perkin-Elmer 2400 CHNS/O series II analyzer.

A Zetasizer nano ZS by Malvern Instruments was used to determine both the hydrodynamic size and zeta potential. Titration experiments were carried out in a Titroline Easy titrator from Schott Instruments between pH 3 and 11 at 20 °C. The temperature was controlled with a Lauda Ecoline RE204 cryostat. Simultaneously, conductimetry measurements were made with a Crison conductimeter 522. For the titrations and zeta-potential measurements, KNO_3 was used as the background electrolyte and HNO_3 and KOH were used to change the pH of the suspensions.

^{57}Fe transmission Mössbauer spectra were recorded in constant acceleration mode at different temperatures using a He closed-cycle cryorefrigerator and a ^{57}Co (Rh) source. The velocity scale was calibrated using an α-Fe foil. The isomer shifts were given with respect to the centroid of the spectrum of α-Fe at room temperature.

3. RESULTS AND DISCUSSION

TEM micrographs of both the as-synthesized laser pyrolysis particles and the acid-treated particles (L and L-AT, respectively) are shown in Figure 1. Both samples presented uniform, spherical
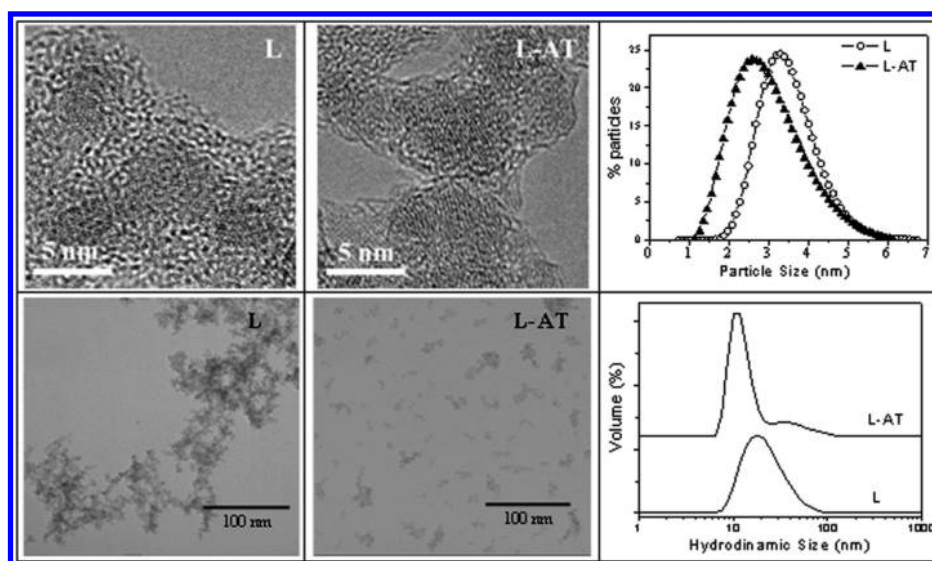
Figure 1. HR-TEM and TEM images of the laser pyrolysis sample before (L) and after (L-AT) acid treatment. On the upper part, discernible lattice fringes were used to determine the iron oxide phase. On the right, the log-normal fit of both the particle size distributions and the hydrodynamic diameter in water of both samples are shown.
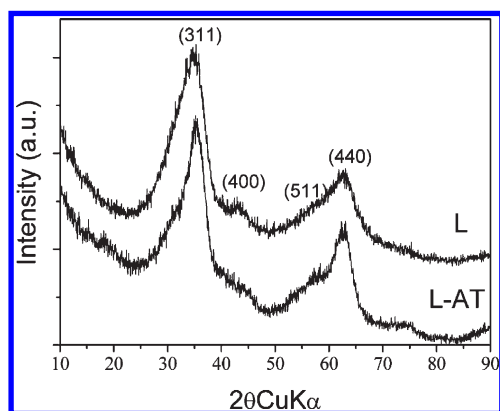
Figure 2. XRD diffraction patterns of the laser pyrolysis samples before (L) and after (LT) acid treatment.

nanoparticles. Particle size diameters calculated from TEM images were 3.5 ± 0.2 and 2.9 ± 0.3 nm for particles before and after acid treatment, respectively.

Apart from the 17% reduction in size of the particles after treatment, these particles seemed to be more disaggregated compared to the original sample (Figure 1). To confirm the nature of the phases, a fast Fourier transform (FFT) analysis of the HR-TEM micrographs was carried out. From the calculated interplanar distances, we verified that the only iron oxide phase present in the treated laser pyrolysis sample (L-AT) was maghemite. This result is consistent with the position and intensity of the XRD peaks. Figure 2 shows the diffractograms of the samples before (L) and after (L-AT) acid treatment. Sample L presented an important peak broadening typical of a disordered structure and very small particles such as those synthesized by laser pyrolysis.[17,30,31] After acid treatment (L-AT), the peaks were slightly sharper, pointing to an increase in the crystal size from 2.5 ± 0.1 nm as seen in sample L to 3 ± 0.1 nm in sample L-AT, which corresponds to approximately 0.5 nm and therefore a 20% increase in size after treatment. This trend is opposite to that

observed by TEM. Consequently, the increase in the crystal size observed by XRD does not involve an increase in particle size but could be related to a structural rearrangement in the particle.

In the case of magnetite particles synthesized by coprecipitation (sample C), the particle size was reduced by acid treatment (from 11 ± 3 to 8 ± 3 nm), which also led to complete oxidation from magnetite (sample C) to maghemite (sample C-AT), confirming the success of the acid treatment in terms of oxidation of the Fe(II) present in the sample.

The partially disordered structure of the laser pyrolysis particles observed by XRD can also be studied by infrared spectroscopy (Supporting Information). The low-frequency region of the infrared spectrum was used to get a general idea of the crystallographic structure of the particles. The broad lattice absorption bands of sample L became narrower after treatment, confirming the increase in crystallinity. Unlike the original sample (L), where the band at 540 cm^{-1} (Fe−O tetrahedral coordination) was more intense than the band at 450 cm^{-1} (Fe−O octahedral coordination), the treated sample (L-AT) presented more intense octahedral coordination bands. This behavior is due to a change in the vacancy ordering during acid treatment.

This change in the tetrahedral and octahedral site distribution observed by FTIR was consistent with the results obtained by Mössbauer spectroscopy (Figure 3). Both samples showed a paramagnetic doublet at 125 K, presented incipient magnetic order at 76 K, and had well-defined magnetic patterns. Therefore, the evaluation of the site distribution was carried out from these latter spectra. Both spectra were fitted by considering two discrete sextets that can be associated with the existence of tetrahedrally coordinated (a sextet with a smaller hyperfine field) and octahedrally coordinated (a sextet with a higher hyperfine field) Fe^{3+} within the spinel-related structure of γ-Fe_2O_3.

Table 1 shows the parameters of the fitting of the two sextets and the areas and the proportion of octahedral and tetrahedral occupied sites ($[Fe^{3+}]_{O_h}/[Fe^{3+}]_{T_d}$). Sample L presented a higher concentration of Fe^{3+} in tetrahedral sites. In the treated sample (L-AT), the area of the sextet pertaining to octahedral sites was
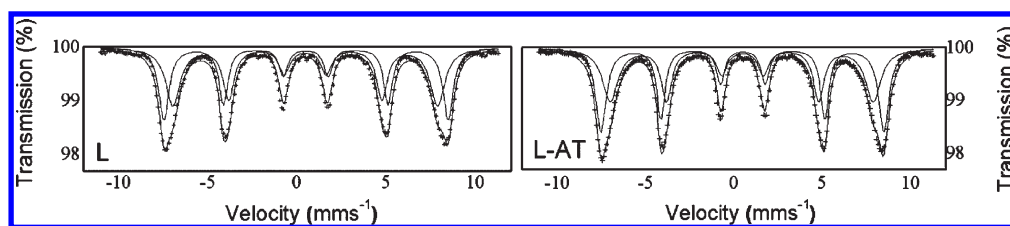
Figure 3. Mössbauer spectra at 15 K of the laser pyrolysis samples before (L) and after (L-AT) acid treatment.

Table 1. Hyperfine Parameters at 15 K for the Coprecipitation and Laser Pyrolysis Samples before (C and L) and after Acid Treatment (C-AT and L-AT), Respectively[a]

	L	L-AT	C	C-AT
δ (mm/s)	0.49	0.49	0.51	0.47
	0.46	0.46	0.42	0.42
Δ or 2ε (mm/s)	0.007	−0.01	−0.004	0.006
	−0.001	−0.03	−0.001	−0.008
H (T)	49.4	49.7	53.2	52.1
	46.0	46.1	51.6	50.2
area (%)	46	52	30	44
	54	48	70	56
$[Fe^{3+}]_{O_h}/[Fe^{3+}]_{T_d}$	0.85	1.08	0.43	0.79

[a] δ is the isomer shift with respect to metallic iron, Δ is the quadrupole splitting (applies to doublets), 2ε is the quadrupole shift (applies to sextets), and H is the hyperfine magnetic field value.

slightly higher than that of the sextet corresponding to tetrahedral sites. Thus, although still far from the ratio $[Fe^{3+}]_{O_h}/[Fe^{3+}]_{T_d} \approx 1.67$, which corresponds to stoichiometric maghemite, acid treatment recrystallized the sample, thereby increasing the structural order. Moreover, at any given temperature between 15 and 76 K (Supporting Information), the hyperfine magnetic fields of sample L-AT were larger and the spectral peaks were narrower than in sample L. Thus, generally speaking, it seems that the crystal size of sample L-AT was slightly greater (and/or the particle size distribution was narrower) than that of sample L.

In the case of the coprecipitation sample, changes in the position and intensity of the FTIR bands were evidence of the change from magnetite (sample C) to maghemite (sample C-AT). Additionally, the Mössbauer spectra of the treated sample showed broader and less-defined sextets than those of the as-prepared sample (Supporting Information). This suggests that particles of sample C-AT were smaller than those of sample C. These results are in good agreement with those obtained by TEM and XRD (data not shown).

To further study the effect of acid treatment on laser pyrolysis particle crystallinity and its relationship to surface disorder, magnetic measurements of the samples before and after acid treatment were carried out. Prior to acid treatment, the laser pyrolysis particles showed an anhysteric magnetization curve at room temperature, which has been previously related to the superparamagnetic behavior of these particles.[32]

Considering the magnetization curves in Figure 4, complete saturation was not reached even for high fields of 50 KOe. This behavior is closely related to the existence of a spin disorder where exchange interactions take place.[17]

However, it is difficult to ascertain whether this disorder is located at the nanoparticle surface (nanoparticles with a crystalline
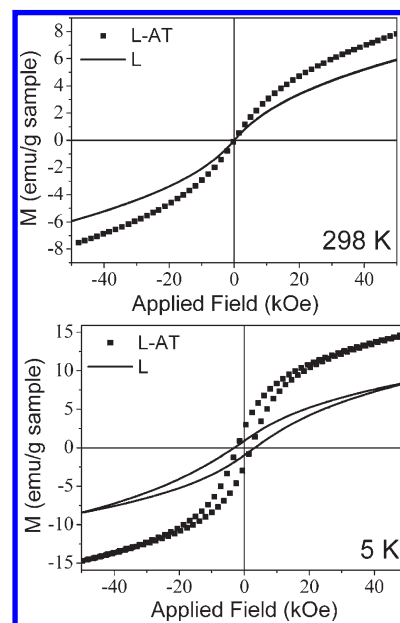

Figure 4. Magnetization curves of the laser pyrolysis samples before (L) and after (L-AT) acid treatment at room temperature and 5 K.

core and a disordered shell) or if the sample is a heterogeneous mixture of crystalline and amorphous (nonordered) nanoparticles. To shed new light on this question, we considered that the existence of a core/shell structure is associated with the presence of an exchange anisotropy.

To look for that phenomenon, the hysteresis loops of the samples at low temperature under an applied field of 5 T were measured. Shifted hysteresis loops and strong magnetic training after cooling the sample in a high field below a certain temperature were observed. This clearly reinforces the idea of a disordered structure at the surface. The field offset from the origin in the shifted hysteresis loops is called the exchange anisotropy field (H_{exc}). The increase in coercivity is related to the extra energy necessary to switch the spins of the ordered part as influenced by the exchange interactions with the frozen disordered part.[17,33]

As previously mentioned, the intimate contact between the ordered and the disordered parts of the particle is an evident requirement for the establishment of exchange anisotropy. Thus, we concluded that the presence of such anisotropy in the nanoparticles synthesized by laser pyrolysis suggests that they are core−shell structures with an ordered crystalline magnetic core and a disordered shell.

The temperature dependence of H_{exc} and H_c for samples before and after acid treatment is shown in Figure 5 and Table 2. H_c and H_{exc} were more than 1 order of magnitude lower for sample L-AT than those obtained for sample L. This fact is
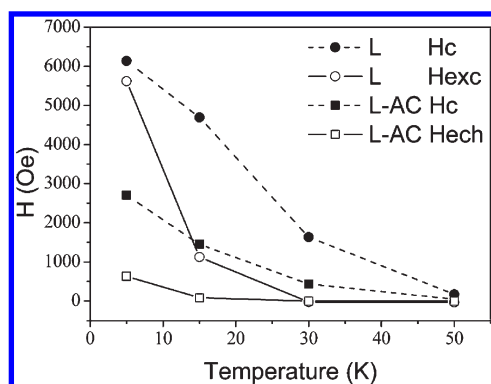
Figure 5. Temperature dependence of H_c and H_{exc} for the laser pyrolysis samples before and after acid treatment.

Figure 6. Zero field cooling-field cooling curves (ZFC-FC) of the laser pyrolysis samples before (L) and after (L-AT) acid treatment.

Table 2. Coercive (H_c) and Exchange Anisotropy (H_{exc}) Fields As a Function of Temperature for the Laser Pyrolysis Samples before (L) and after Acid Treatment (L-AT)

T (K)	H_c (Oe)		H_{exc} (Oe)	
	L	L-AT	L	L-AT
5	6133	2703	5616	633
15	4690	1447	1124	85
30	1633	436	0	0
50	170	50	0	0

Table 3. Summary of the Results from Magnetic Measurements at Room Temperature and 5 K for the Laser Pyrolysis Samples before (L) and after Acid Treatment (L-AT)[a]
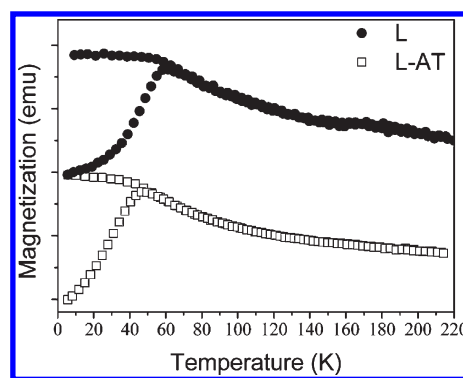
T (K)	M_s (emu/g sample)		χ (emu/g sample·kOe)		H_c (Oe)	
	L	L-AT	L	L-AT	L	L-AT
5	14	20	0.26	1.16	3150	2130
298	9	12	0.25	0.37	0	0

[a] Saturation magnetization (M_s), initial susceptibility (χ), and coercivity (H_c).

related to a higher disordered proportion in the sample before treatment. It strongly indicates that the disordered shell is recrystallized during acid treatment, increasing the corelike percentage and reducing the exchange anisotropy. This also explains the larger saturation magnetization of the acid-treated particles (Table 3).

We remark that no significant differences in exchange anisotropy were observed for the coprecipitated particles before and after acid treatment. This is related to the lower surface disorder in the samples synthesized by coprecipitation compared to the laser pyrolysis samples, although it was higher than the surface disorder of samples prepared by other synthesis routes at higher temperatures and in the presence of surfactants.[34]

Zero field cooling-field cooling (ZFC-FC) curves of the laser pyrolysis samples before and after treatment were measured for dilute frozen dispersions ([Fe_2O_3] = 0.025% w/w) to minimize the effect of dipolar interparticle interactions. ZFC-FC curves for samples L and L-AT are shown in Figure 6. The ZFC curve shows wide maxima at about T_M = 60 and 50 K for L and L-AT,

respectively. The ZFC and FC curves for both samples are superimposed just after T_M, as the superparamagnetic regime was reached. For particles of the same volume, a decrease in T_M could be related to a reduction in dipolar interactions. As observed by TEM (Figure 1), this reduction in dipolar interactions is due to a reduction in the nanoparticle aggregation in the aqueous dispersion. To confirm the reduction of the interparticle interactions, T^* was obtained from the ZFC-FC curve of the treated particles (as described elsewhere[35]). T^*, a phenomenological parameter that added to the temperature in the Langevin function, describes the effect of dipolar interactions in an interacting superparamagnetic regime. For the treated sample, T^* was only 10 K, less than half of the value in the original sample ($T^* \approx 25$ K), which is a consequence of a reduction in interparticle interactions.

From these results, it is clear that the recrystallization of particles is especially relevant on the surface and therefore is expected to affect the colloidal behavior of the particles. This behavior was studied in terms of the aggregate size, isoelectric point (IEP), and surface charge density (σ_0).

The aggregate size of the laser pyrolysis and coprecipitated samples before and after acid treatment was measured by dynamic light scattering (DLS). In both cases, a decrease in the average aggregate size at pH 3 was observed after acid treatment. Thus, in the samples synthesized by laser pyrolysis, the aggregate size decreased from 18 nm (sample L) to 10 nm (sample L-AT) (Figure 1), and in the case of particles synthesized by coprecipitation, the aggregate size was reduced from 80 nm (sample C) to 30 nm (sample C-AT) (data not shown). In light of the TEM and DLS results, the aggregate size of the dispersions was drastically reduced via acid treatment. This is of paramount importance when biomedical applications are pursued because the aggregate size is one of the key parameters in terms of pharmacokinetics, biodistribution, and toxicity. To complete the colloidal characterization of the samples, the determination of the isoelectric point (IEP) was carried out. The zeta potential versus pH for samples synthesized by laser pyrolysis and coprecipitation is plotted in Figure 7.

In both samples, there was a shift in the IEP to higher values with acid treatment. This change is due to modifications on the particle surface, which can originate from various interrelated factors such as the increase in $[Fe^{3+}]_{O_h}/[Fe^{3+}]_{T_d}$ with a subsequent increase in the basicity of the Fe−OH surface groups' rearrangement of the surface structure, changes in the degree of hydration, or changes in the impurity content. Previous studies
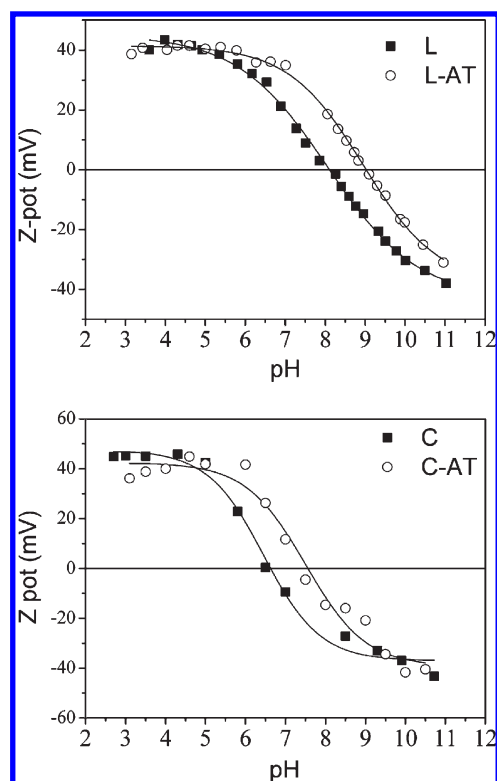
Figure 7. Measurements of the IEP (zeta potential as a function of pH) before and after acid treatment for samples synthesized by laser pyrolysis (L and L-AT) and coprecipitation (C and C-AT). The background electrolyte (KNO_3) concentration was 10^{-2} M in both cases.

Figure 8. pH dependence of the surface charge density for the coprecipitated samples before (C) and after (C-AT) acid treatment.

have shown that treatments leading to an increase in surface hydration result in a more basic IEP.[36] In this work, we reported evidence of the modification of the proportion of octahedral Fe(III) by Mössbauer spectroscopy. In addition, thermogravimetric analysis (Supporting Information) provided clear evidence of an increase in the degree of hydration in the treated sample (10% weight loss at 400 °C in sample L and 23% in sample L-AT). Additionally, the increase in crystallinity observed by XRD and TEM pointed to a rearrangement in the crystal structure that should affect the particle surface as well. Finally, CHN chemical analysis showed a reduction in carbon impurities with treatment from 2 to 0.4% for samples L and L-AT, respectively. With these results, we can conclude that several factors lead to the increase in the number of basic Fe−OH surface groups responsible for the IEP shift to higher values with acid treatment.

The experimental value of the IEP of sample C (6.5) is in good agreement with those previously reported in the literature for magnetite.[37] Because the surfaces of particles synthesized by coprecipitation have been widely studied in the past, we have chosen these particles for the determination of surface charge density in order to compare the obtained values for the acid-treated samples with those reported previously in the literature.

The surface charge density (σ_0) was determined over a wide pH range to obtain a better understanding of the surface structure and charge modifications due to acid treatment. For metal oxides and related materials, σ_0 is determined by potentiometric titration. However, this kind of titration is highly dependent on the experimental conditions, such as the nature and concentration of the background electrolyte, the temperature,
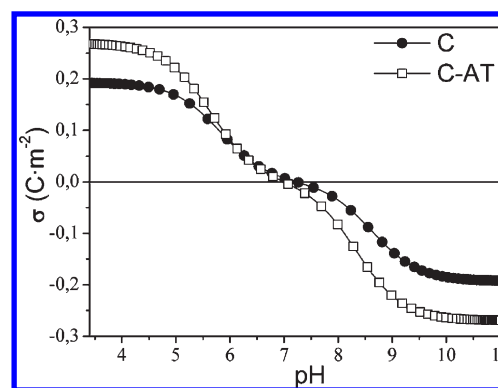
silica and carbonate adsorption, and even the type of interpolation used in the graph.[38] To overcome these problems, simultaneous conductometric and potentiometric titrations (SCPT) were performed. Conductimetric curves allow for easier identification of the linear intervals for a more accurate determination of σ_0 with the 2-pK model, as reported previously by other authors.[39,40]

Figure 8 shows the pH dependence of the surface charge density (σ_0). The treated sample presented higher charge density values below pH 5.5 and above pH 7.5. However, for extreme values of pH, the high ionic strength did not allow stable colloidal dispersions, even though the particle surface was completely charged. Around pH values of 4 and 10.5, where the surface is charge-saturated, samples C and C-AT presented surface charge densities of 0.192 and 0.267 C/m², respectively. This means that the treated particles presented a surface charge density that was almost 5 times greater than those reported before.[41] These highly charged surfaces ease further particle coating to stabilize iron oxide nanoparticles at physiological pH.[42] This significant increase in the surface charge points to the hydration and activation of the particle surface during acid treatment.

The main mechanism for explaining the increase in charge and crystallinity and the reduction in surface disorder is based on dissolution−recrystallization phenomena. In the first step of treatment, particles are partially dissolved. This dissolution progresses further when particles are smaller or more amorphous or when the concentration of acid is higher. This dissolution phenomenon is consistent with the reduction in particle size characterized by TEM. Afterward, Fe^{3+} is introduced into the system as an $Fe(NO_3)_3$ salt. Part of this Fe^{3+} can recrystallize on the particle surface, thus increasing the crystal size slightly and improving the particle crystallinity. Because of the treatment conditions, the disordered layer on the particle surface may also rearrange itself, increasing its crystalline order independently of the presence of Fe^{3+} in solution.

Fe^{3+} in solution in acid media forms hexa-aquo ion $Fe(H_2O)_6^{3+}$. The hydrolysis of this ion is favored by an increase in pH, by heating, or by dilution. Thus, the addition of water and heating in the second step of the treatment and the subsequent washing process lead to the formation of $Fe(H_2O)_n(OH)_m^{3-m}$. This process is stepwise and might lead to the formation of an iron polymer as previously described.[43,44] This polymer can result in different secondary iron oxide/hydroxide phases depending on the pH, temperature, or the presence of certain cations[45] and also can result in an external active layer, as seen in this work.

Note that the recrystallization phenomenon was only observed for treated particles smaller than 5 nm. Larger particles are difficult to dissolve and are thermodynamically more stable.[46] Nevertheless, the relevance of surface disorder becomes smaller as the particle size increases and eventually disappears for large enough particles. Thus, the acid treatment effect reported in this work is significant only when improving ultrasmall nanoparticles with poor magnetic properties and low colloidal stability in an aqueous medium.

4. CONCLUSIONS

We have developed a chemical protocol consisting of an acid treatment to improve the colloidal and magnetic properties of ultrasmall iron oxide nanoparticles prepared by laser pyrolysis via a reduction of the surface disorder. A complete characterization of the particles before and after acid treatment was carried out. We have concluded that the dissolution of the disordered layer at the particle surface and further recrystallization of an iron polymer activates the surface and prepares the particles for further functionalization with bioactive ligands. After acid treatment, particles presented smaller aggregate sizes, larger surface charge densities, and better colloidal stability, which in short represent an enhancement in the colloidal properties. In addition to that, the saturation magnetization (M_s) was increased by 40% and the initial susceptibility was drastically enhanced with respect to that of the as-prepared sample. Moreover, the exchange anisotropy field was significantly diminished, providing evidence of a reduction in surface disorder.

■ ASSOCIATED CONTENT

⑤ Supporting Information. Mössbauer and FTIR spectra of the coprecipitation and laser pyrolysis samples before and after acid treatment. Thermogravimetrical analysis of the laser pyrolysis samples before and after acid treatment. This material is available free of charge via the Internet at http://pubs.acs.org.

■ AUTHOR INFORMATION

Corresponding Author
*Tel: +34913349061. Fax: +34913720623. E-mail: sabino@icmm.csic.es.

■ ACKNOWLEDGMENT

■ REFERENCES

(1) Tartaj, P.; Morales, M. P.; Gonzalez-Carreño, T.; Veintemillas-Verdaguer, S.; Serna, C. J. *J. Magn. Magn. Mater.* **2005**, *290−291*, 28–34.

(2) Tartaj, P. *Curr. Nanosci.* **2006**, *2*, 43–53.

(3) Corot, C.; Robert, P.; Idee, J. M.; Port, M. *Adv. Drug Delivery Rev.* **2006**, *58*, 1471–1504.

(4) Gupta, A. K.; Gupta, M. *Biomaterials* **2005**, *26*, 3995–4021.

(5) Goya, G. F.; Grazu, V.; Ibarra, M. R. *Curr. Nanosci.* **2008**, *4*, 1–16.

(6) Mahmoudi, M.; Sahraian, M. A.; Shokrgozar, M. A.; Laurent, S. *ACS Chem. Neurosci.* **2011**, *2*, 118–140.

(7) Cho, E. C.; Glaus, C.; Chen, J.; Welch, M. J.; Xia, Y. *Trends Mol. Med.* **2010**, *16*, 561–573.

(8) Figuerola, A.; Di Corato, R.; Manna, L.; Pellegrino, T. *Pharmacol. Res.* **2010**, *62*, 126–143.

(9) Garrido-Ramirez, E. G.; Theng, B. K. G.; Mora, M. L. *Appl. Clay Sci.* **2010**, *47*, 182–192.

(10) Auffan, M.; Rose, J.; Bottero, J. Y.; Lowry, G. V.; Jolivet, J. P.; Wiesner, M. R. *Nat. Nanotechnol.* **2009**, *4*, 634–641.

(11) Theron, J.; Walker, J. A.; Cloete, T. E. *Crit. Rev. Microbiol.* **2008**, *34*, 43–69.

(12) Lu, A. H.; Salabas, E. L.; Schuth, F. *Angew. Chem., Int. Ed.* **2007**, *46*, 1222–1244.

(13) Tronc, E.; Jolivet, J. P.; Massart, R. *Mater. Res. Bull.* **1982**, *17*, 1365–1369.

(14) Tronc, E.; Jolivet, J. P. *Hyperfine Interact.* **1986**, *28*, 525–528.

(15) Morales, M. P.; Andres-Verges, M.; Veintemillas-Verdaguer, S.; Montero, M. I.; Serna, C. J. *J. Magn. Magn. Mater.* **1999**, *203*, 146–148.

(16) Serna, C. J.; Bødker, F.; Mørup, S.; Morales, M. P.; Sandiumenge, F.; Veintemillas-Verdaguer, S. *Solid State Commun.* **2001**, *118*, 437–440.

(17) Morales, M. P.; Veintemillas-Verdaguer, S.; Montero, M. I.; Serna, C. J.; Roig, A.; Casas, L. I.; Martinez, B.; Sandiumenge, F. *Chem. Mater.* **1999**, *11*, 3058–3064.

(18) Roduner, E. *Chem. Soc. Rev.* **2006**, *35*, 583–592.

(19) Guardia, P.; Batlle-Brugal, B.; Roca, A. G.; Iglesias, O.; Morales, M. P.; Serna, C. J.; Labarta, A.; Batlle, X. *J. Magn. Magn. Mater.* **2007**, *316*, E756–E759.

(20) Areias, F. M.; Rego, A. C.; Oliveira, C. R.; Seabra, R. M. *Biochem. Pharmacol.* **2001**, *62*, 111–118.

(21) Goswami, T.; Rolfs, A.; Hediger, M. A. *Int. J. Biochem. Cell Biol.* **2002**, *80*, 679–689.

(22) Veintemillas-Verdaguer, S.; Del Puerto Morales, M.; Bomati-Miguel, O.; Bautista, C.; Zhao, X.; Bonville, P.; De Alejo, R. P.; Ruiz-Cabello, J.; Santos, M.; Tendillo-Cortijo, F. J.; Ferreiros, J. *J. Phys. D: Appl. Phys.* **2004**, *37*, 2054–2059.

(23) Van Ewijk, G. A.; Vroege, G. J.; Philipse, A. P. *J. Magn. Magn. Mater.* **1999**, *201*, 31–33.

(24) Bee, A.; Massart, R.; Neveu, S. *J. Magn. Magn. Mater.* **1995**, *149*, 6–9.

(25) Tourinho, F. A.; Franck, R.; Massart, R. *J. Mater. Sci.* **1990**, *25*, 3249–3254.

(26) Gomes, J. D. A.; Sousa, M. H.; Tourinho, F. A.; Aquino, R.; Da Silva, G. J.; Depeyrot, J.; Dubois, E.; Perzynski, R. *J. Phys. Chem. C* **2008**, *112*, 6220–6227.

(27) Massart, R.; Dubois, E.; Cabuil, V.; Hasmonay, E. *J. Magn. Magn. Mater.* **1995**, *149*, 1–5.

(28) Massart, R. *IEEE Trans. Magn.* **1981**, *MAG-17*, 1247–1248.

(29) Veintemillas-Verdaguer, S.; Morales, M. P.; Serna, C. J. *Mater. Lett.* **1998**, *35*, 227–231.

(30) Veintemillas-Verdaguer, S.; Morales, M. P.; Serna, C. J. *Appl. Organomet.* **2001**, *15*, 365–372.

(31) Veintemillas-Verdaguer, S.; Bomati-Miguel, O.; Morales, M. P. *Scr. Mater.* **2002**, *47*, 589–593.

(32) Morales, M. P.; Veintemillas-Verdaguer, S.; Serna, C. J. *J. Mater. Res.* **1999**, *14*, 3066–3072.

(33) Zheng, R. K.; Wen, G. H.; Fung, K. K.; Zhang, X. X. *Phys. Rev. B* **2004**, *69*.

(34) Roca, A. G.; Morales, M. P.; O'Grady, K.; Serna, C. J. *Nanotechnology* **2006**, *17*, 2783–2788.

(35) Allia, P.; Coisson, M.; Tiberto, P.; Vinai, F.; Knobel, M.; Novak, M. A.; Nunes, W. C. *Phys. Rev. B* **2001**, *64*, 144420.

(36) Parks, G. A. *Chem. Rev.* **1965**, *65*, 177–198.

(37) Kosmulski, M. *J. Colloid Interface Sci.* **2002**, *253*, 77–87.

(38) Kosmulski, M., Ed.; *Surface Charging and Points of Zero Charge*; Surfactant Science Series; CRC Press: Boca Raton, FL, 2009; Vol. 145.

(39) Campos, A. F. C.; Tourinho, F. A.; Da Silva, G. J.; Lara, M. C. F. L.; Depeyrot, J. *Eur. Phys. J. E* **2001**, *6*, 29–35.

(40) European Colloid and Interface Society; *Trends in Colloid and Interface Science XVII*; Cabuil, V., Levitz, P., Treiner, C., Eds.; Progress in Colloid and Polymer Science; Springer: Berlin, 2004; Vol. 126.

(41) Garcell, L.; Morales, M. P.; Andres-Verges, M.; Tartaj, P.; Serna, C. J. *J. Colloid Interface Sci.* **1998**, *205*, 470–475.

(42) Mejias, R.; Costo, R.; Roca, A. G.; Arias, C. F.; Veintemillas-Verdaguer, S.; Gonzalez-Carreño, T.; del Puerto Morales, M.; Serna, C. J.; Mañas, S.; Barber, D. F. *J. Controlled Release* **2008**, *130*, 168–174.

(43) Schneider, W.; Schwyn, B. *The Hydrolysis of Iron in Synthetic, Biological and Aquatic Media*; Wiley Interscience: New York, 1987.

(44) Jolivet, J. P.; Froidefond, C.; Pottier, A.; Chaneac, C.; Cassaignon, S.; Tronc, E.; Euzen, P. *J. Mater. Chem.* **2004**, *14*, 3281–3288.

(45) Welo, L. A.; Baudisch, O. *Chem. Rev.* **1934**, *15*, 45–97.

(46) Navrotsky, A.; Mazeina, L.; Majzlan, J. *Science* **2008**, *319*, 1635–1638.